ACS Sustainable Chemistry & Engineering

pubs.acs.org/journal/ascecg

Research Article

Stable Ti^{3+} Sites Derived from the Ti_xO_y-P_z Layer Boost Cubic Fe_2O_3 for Enhanced Photocatalytic N_2 Reduction

Wensheng Zhang, Dongfang Han, Mengjiao Dai, Yingying Fan, Guoliang Pan, Weiqi Liang, Qitong Zheng, Dongdong Qin, Dongxue Han,* Ying He,* and Li Niu

Cite This: https://doi.org/10.1021/acssuschemeng.1c05890

Read Online

ACCESS | Metrics & More | Article Recommendations | Supporting Information

ABSTRACT: Photocatalytic N_2 fixation to NH_3 using water as the reductant constitutes an encouraging method for synthesized ammonia (NH_3) in the future, which helps to discover efficient photocatalysts for improving the sunlight utilization as well as enhancing the catalytic efficiency to N_2 fixation. Hematite (α-Fe_2O_3), a high-stability, low-cost, natural abundance semiconductor photocatalyst, could represent a promising candidate for visible-light-driven N_2-to-NH_3 conversion in terms of cost-effectiveness, while the related reports are still sparse in this field. Notably, the single α-Fe_2O_3 photocatalyst generally suffers from a low reduction ability of photogenerated electrons; fatal electron–hole recombination and restricted surface active sites limit its photocatalytic activity specific potential N_2 fixing. To solve the issues mentioned above, here, we designed a surface phosphorus doping anatase TiO_2 (Ti_xO_y-P_z) layer containing stable Ti^{3+} sites for improving the photocatalytic N_2 reduction reaction (pNRR) performance of cubic α-Fe_2O_3. The unsaturated Ti^{3+} species were induced on the Ti_xO_y-P_z layer as active sites by PH_3 treating to realize high adsorption and activation of the N_2 molecules. Meanwhile, some titanium metal defects formed by phosphorus doping make the structure of the catalyst more stable. Moreover, both TPD and time-resolved PL decay data prove that the Ti^{3+} species of Fe_2O_3@Ti_xO_y-P_z are active sites for N_2 chemical absorption as well as N≡N triple bond cleavage. Using the advantage of surface Ti^{3+} sites of the Ti_xO_y-P_z layer together with interfacial coupling regarding Fe_2O_3@Ti_xO_y-P_z nanohybrid catalysts, N_2 can be effectively photoreduced to NH_3 with illumination under environmental conditions. For the N_2 photoreduction using an Fe_2O_3@Ti_xO_y-P_z nanohybrid, the NH_4^+ yield velocity rate is 15.65 μmol $g_{cat.}^{-1}$ h^{-1}, which is 9.43-fold, 5.31-fold, 8.37-fold, and 2.95-fold higher than cubic Fe_2O_3, Fe_2O_3@TiO_2, Fe_2O_3-P_z, and Ti_xO_y-P_z, respectively. Satisfactorily, the as prepared Fe_2O_3@Ti_xO_y-P_z has quite good stability, and the NH_3 production was still remarkably unvaried in six cycling tests. This work contributes to a feasible way for designing and synthesizing nanocomposite materials which have excellent photocatalytic N_2 fixation performance.

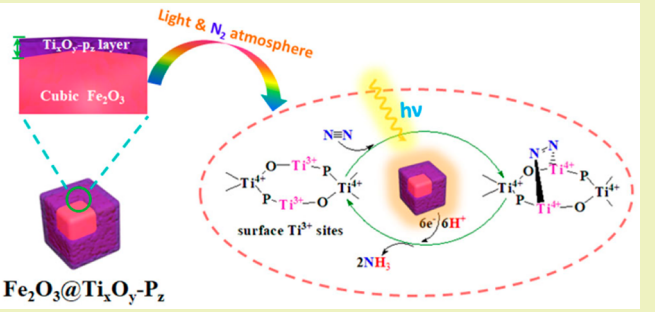

KEYWORDS: *Hematite, Surface phosphorus doping anatase TiO_2 layer, Photocatalytic N_2 reduction reaction, Stable Ti^{3+} sites*

INTRODUCTION

Ammonia (NH_3) is an indispensable chemical applied in modern society and is the basic component for the manufacturing of synthetic chemicals like drugs, fertilizers, resins, dyes, and explosives.[1−3] When being condensed into liquid, it exhibits a higher energy density and transportability compared with hydrogen (H_2) and thus can be used for power fuel cells in the short run.[4,5] So far, the industrial fabrication of ammonia from nitrogen (N_2) fixing is through the Haber–Bosch process depending on high pressure and temperature.[6,7] Such a process consuming intensive resource and energy needs complicated large-scale infrastructure, which also generates a large amount of carbon dioxide.[8,9] As the demand for NH_3 grows, it is necessary to develop a less energy-consuming alternative for N_2 fixation that is more green and sustainable.[10,11]

The photocatalytic N_2 reduction reaction (pNRR), taking H_2O as a proton source, drives the N_2-to-NH_3 reduction under the assistance of a semiconductor photocatalyst and renewable solar energy, and thus has become a new research field attracting researchers recently.[12,13] When it comes to using sunlight efficiently, an ideal photocatalyst shall be capable of absorbing visible light, as the solar spectrum is composed of a huge proportion of visible light (about 44%).[14] As promising visible-light-responsive catalysts, hematite (α-Fe_2O_3) exhibits a strong stability, low cost, wide visible-light response, natural

Received: August 28, 2021
Revised: October 16, 2021

abundance, and environmentally friendliness and has been well concerned.[15,16] Nevertheless, in single component α-Fe_2O_3 materials, its photogenerated electrons have low reduction ability so that an effective pNRR reaction cannot occur. Furthermore, the remarkable photoinduced electron−hole recombination velocity impedes its broad utilization in pNRR. Therefore, it is challenging to overcome the natural limitations of α-Fe_2O_3, for developing a highly efficient photocatalyst driven by both ultraviolet and visible light irradiation.

Under sunlight, many electrons can achieve the VB-to-CB excitation, even to the empty bands above the CB bottom.[17,18] All of those high-energy-level electrons (HELEs) can rapidly relax to the CB bottom on a milli-microsecond-level time scale and lose the potential energy largely. Remarkably, they can be utilized by virtue of a HELE platform, and the platform can maintain enough potential energy of these electrons as well as prolong their charge lifetime. As confirmed by previous research, wide band gap semiconductors like titanium dioxide (TiO_2) which has a negative CB provide an HELE platform for α-Fe_2O_3, enhancing the charge separation, prolonging the charge lifetime, as well as strengthening photocatalytic activities.[19,20] Accordingly, a vital step of using visible-light-excited HELEs lies in the introduction of a proper electron-accepting platform which has excellent catalytic capability specific to reduction actions.

In other aspects, TiO_2 is broadly used in terms of pNRR owing to its good stability, low cost, as well as nontoxicity.[21,22] Guth and Schrauzer for the first time discovered the ability of TiO_2 powder for N_2-to-NH_3 reduction under ultraviolet illumination in 1977.[23] Nowadays, the introduction of defects into the crystal lattices of TiO_2 for forming unsaturated Ti^{3+} sites as well as surface oxygen vacancies (OVs) can remarkably enhance the N_2 adsorption and N≡N triple bond activation.[24−26] For instance, the Hirakawa group found the hydrogen-reduced TiO_2 (name JRC-TIO-6) can generate NH_3 (3.81 μmol g^{-1} h^{-1}) via ultraviolet light successfully, which exhibits a larger efficiency relative to other kinds of commercially available TiO_2 nanoparticulates (P25, 3.04 μmol g^{-1} h^{-1}) for pNRR.[27] Nevertheless, the hydrogen-treated process can be hardly controlled, as it has huge danger. Also, the post-treating methods, like the reduction with hydrogen, hydrazine, or sodium borohydride, usually produce Ti^{3+} species on the superficial region, which are unstable in photocatalysis reactions.[28] A reliable approach for introducing appropriate Ti^{3+} species into the TiO_2 nanolayer with satisfactory controllable properties and stability for boosting the pNRR activity of α-Fe_2O_3, therefore, seems to be imperative.

Herein, we designed stable Ti^{3+} defects and a surface phosphorus doping anatase TiO_2 (Ti_xO_y-P_z) layer for improving the pNRR performance of cubic α-Fe_2O_3. The unsaturated Ti^{3+} species were used on the anatase TiO_2 layer as active sites by PH_3 treatment to realize remarkable absorption and activation of the N_2 molecules. At the same time, the existence of Ti^{3+} casts a vital effect on the photocatalytic activity. In contrast to cubic Fe_2O_3, Fe_2O_3@TiO_2, Fe_2O_3-P_z, and Ti_xO_y-P_z, the as-designed Fe_2O_3@Ti_xO_y-P_z samples exhibit an enhanced photocatalytic N_2 fixation rate. Moreover, Fe_2O_3@Ti_xO_y-P_z samples displayed satisfactory photochemistry steadiness as well. In addition, the probable reaction mechanism was put forward as well. We envisage that our work presents a practical method to uplift the photocatalytic activity of narrow band gap semiconductors (e.g., α-Fe_2O_3) by coupling the wide band gap semiconductor nanolayer with rich active sites.

EXPERIMENTAL SECTION

Materials and Reagents. Iron(III) chloride hexahydrate ($FeCl_3$·$6H_2O$) and sodium hypophosphite (NaH_2PO_2) were purchased from Beijing Innochem Reagents Co., Ltd. Potassium hydroxide (KOH) and absolute ethanol (C_2H_5OH) were bought from Sinopharm Chemical Company. Tetrabutyl titanate (TBOT), poly(*n*-vinyl-pyrrolidone) K-30 (PVP), labeled $^{15}N_2$ gas, phenol nitroprusside liquor, and alkaline hypochlorite liquor were bought from Sigma-Aldrich Chemical Co. NH_4Cl (99.8%) was from Shanghai Merck Chemical Technology Company. The entire reagents were of analysis purity (AR) and utilized as received with no further purifying. Deionization water (18.25 Ω) was utilized during the experiments.

Apparatus. X-ray diffraction (XRD) features of the samples were documented on a PANalytical diffraction meter via Cu irradiation. The morphologies and element compositions were investigated via scanning electron microscopy (SEM, JEOL JSM-7001F) and transmission electron microscopy (TEM, JEOL 2100F). The absorption spectra were obtained using diffuse reflection spectroscopy (DRS, HITACHI UV-3900). The photochemical reactor was installed on the CEL-GPPcL system (Beijing China Education Au-light Company) with a 300 W Xe lamp. The chemisorbed N_2 was used in N_2 temperature-programmed desorption experiments (Micromeritics Auto Chem II) using TCD as a detector. The surface electronic states were analyzed via X-ray photoelectron spectroscopy (XPS, Thermo ESCALAB 250Xi) with the entire binding energy associated with the C 1s peak at 284.6 eV. Mott−Schottky plots were carried out via an electrochemical workstation (CHI Instruments CHI760-1). Steady and transient photoluminescence (PL) curves of the as-prepared samples were acquired on a FLS1000 fluorescent lifetime spectral photometer (Edinburgh Instruments, U.K.) excited by a hydrogen flashlight under a wavelength of 800 nm. The various monochromatic light sources including PLS-LED365 nm, PLS-LED420 nm, PLS-LED470 nm, PLS-LED535 nm, and PLS-LED630 nm were purchased from Beijing PerfectLight Technology Co., Ltd. The percentages of Fe, Ti, and P within the samples were identified by atomic absorption spectroscopy (AAS, Varian SpectrAA 220FS) and inductively coupled plasma optical emission spectroscopy (ICP-OES, PerkinElmer Optima 4300DV), separately.

Photocatalytic Nitrogen Fixation. The photocatalytic N_2-fixation NH_3 synthetic assay was finished in the self-assembled photocatalysis reaction platform, as demonstrated in Figure S2. The photocatalytic N_2 fixation is achieved on the three-phase interface, including N_2 in the gas, H_2O in the liquid, and the catalyzer in the solid phase. Synthesis NH_3 property assays were completed under room temperature and atmosphere pressure. A 300 W Xe lamp (full-spectrum, 463 mW·cm^{-2}) was utilized as the illuminant and 10 cm away from the illuminant to the fluid level. First, 40 mg of photocatalyst was dispersed in 200 mL of deionized water in a cell equipped with water circulation. Second, the mix was continuously agitated without light and with highly purified N_2 bubbled under a flow velocity of 200 mL·min^{-1} for 30 min; then, the light was turned on and 4.0 mL of reactive medium was taken out from the reaction every 30 min. The reaction mixture was purified by removing the photocatalyst by using the 0.22 μm filter. The obtained solution was used for further analysis.

Determination of NH_3. The NH_3 in the photocatalytic reaction solution was quantified by the indophenol approach according to previous work.[29] In order to calibrate in aqueous electrolytes, a given NH_4Cl concentration was supplemented into 0.1 M KOH and afterwards subjected to neutralization via supplementing 0.5 M H_2SO_4. A 0.5 mL portion of phenol nitroprusside liquor and a 0.5 mL portion of alkaline hypochlorite liquor were subsequently supplemented into 2.0 mL of the treated specimen. The liquor was incubated for 30 min under room temperature without light, and the sample absorbance was analyzed by the UV−vis spectroscopic

https://doi.org/10.1021/acssuschemeng.1c05890
ACS Sustainable Chem. Eng. XXXX, XXX, XXX−XXX

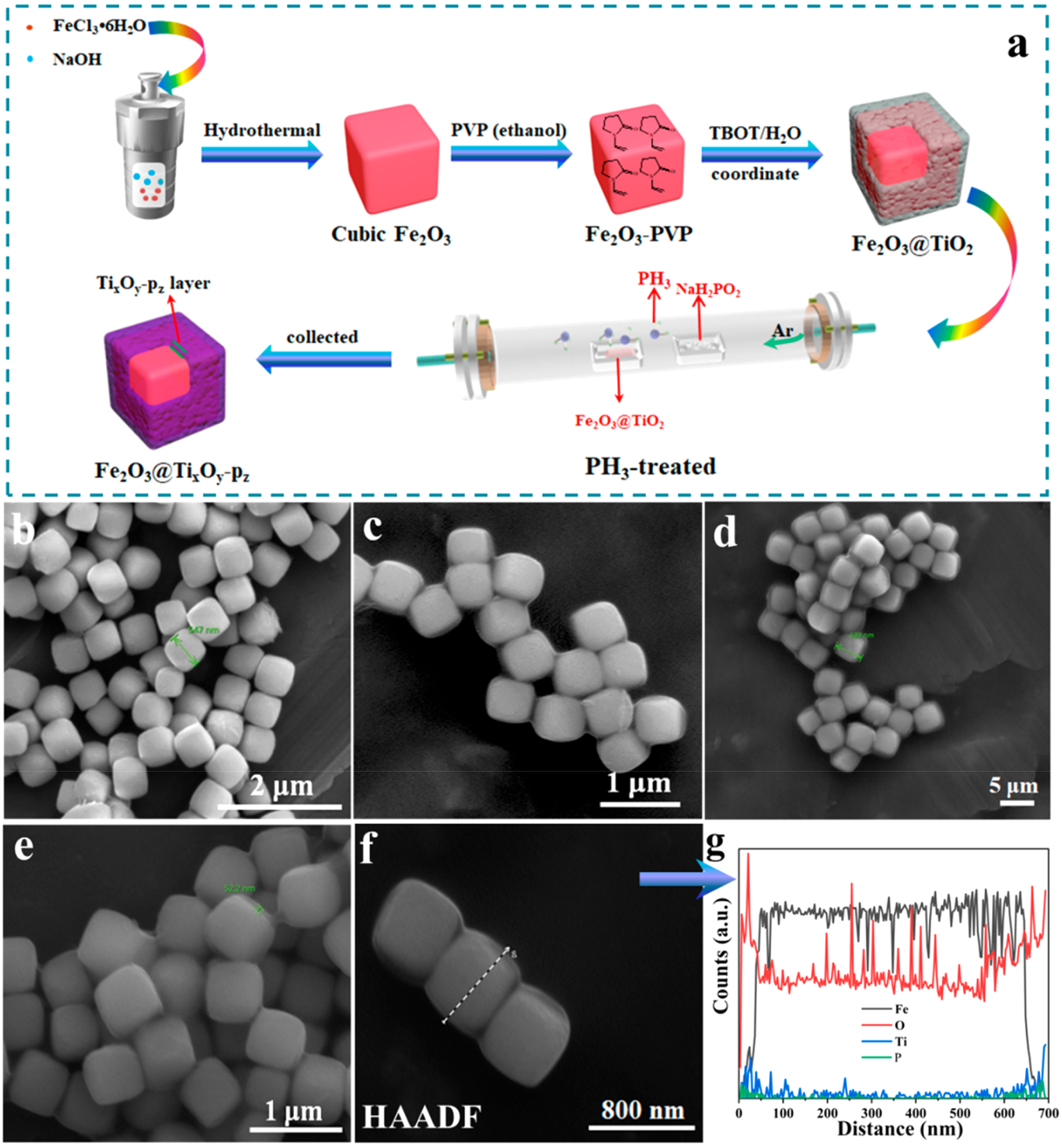

Figure 1. (a) Diagram of the experiment process for fabrication of Fe_2O_3@Ti_xO_y-P_z photocatalysts. SEM imaging of cubic Fe_2O_3 (b), Fe_2O_3@TiO_2 (c), and Fe_2O_3@Ti_xO_y-P_z (d) and in higher resolution of Fe_2O_3@Ti_xO_y-P_z (e). The HAADF image of Fe_2O_3@Ti_xO_y-P_z (f) and the corresponding EDS line scan curves (g).

method (UV-17800, Shimadzu). The correction curve was established for NH_3 with the following data: 0, 0.01, 0.05, 0.1, 0.5, 1.0, 5.0, 10, and 50 μmol^{-1} L^{-1}. The fit curve of the absorption peak of every thickness presented a linearity regression with an R^2 value of 0.99974 (see Figure S3).

$^{15}N_2$ Isotope Labeling Experiments. Labeled $^{15}N_2$ was bought from Sigma-Aldrich Chemical Co., Ltd. It was employed to verify that the identified NH_3 originates from N_2. A low-speed gaseous flow system was utilized owing to the limited supply and expensiveness of $^{15}N_2$. First, 20 mg of photocatalyst was dispersed in 100 mL of deionization water in a cell equipped with water circulation. Second, the mixture was continuously agitated without light and with highly purified N_2 bubbled under a flow velocity of 100 mL·min^{-1} for 10 min. Then, the light was turned on and 4.0 mL of reactive medium was taken out from the reaction every 30 min with further removal of the photocatalyst by using the 0.22 μm filter. Estimation of the obtained $^{15}NH_4^+$ was done indirectly using the indophenol method, due to the low mass of $^{15}NH_4^+$ for LC-MS research. The preparation of the samples for LC-MS assay was displayed below: 0.5 mL of phenol nitroprusside liquor (P6994, Sigma-Aldrich) and 0.5 mL of

https://doi.org/10.1021/acssuschemeng.1c05890
ACS Sustainable Chem. Eng. XXXX, XXX, XXX−XXX

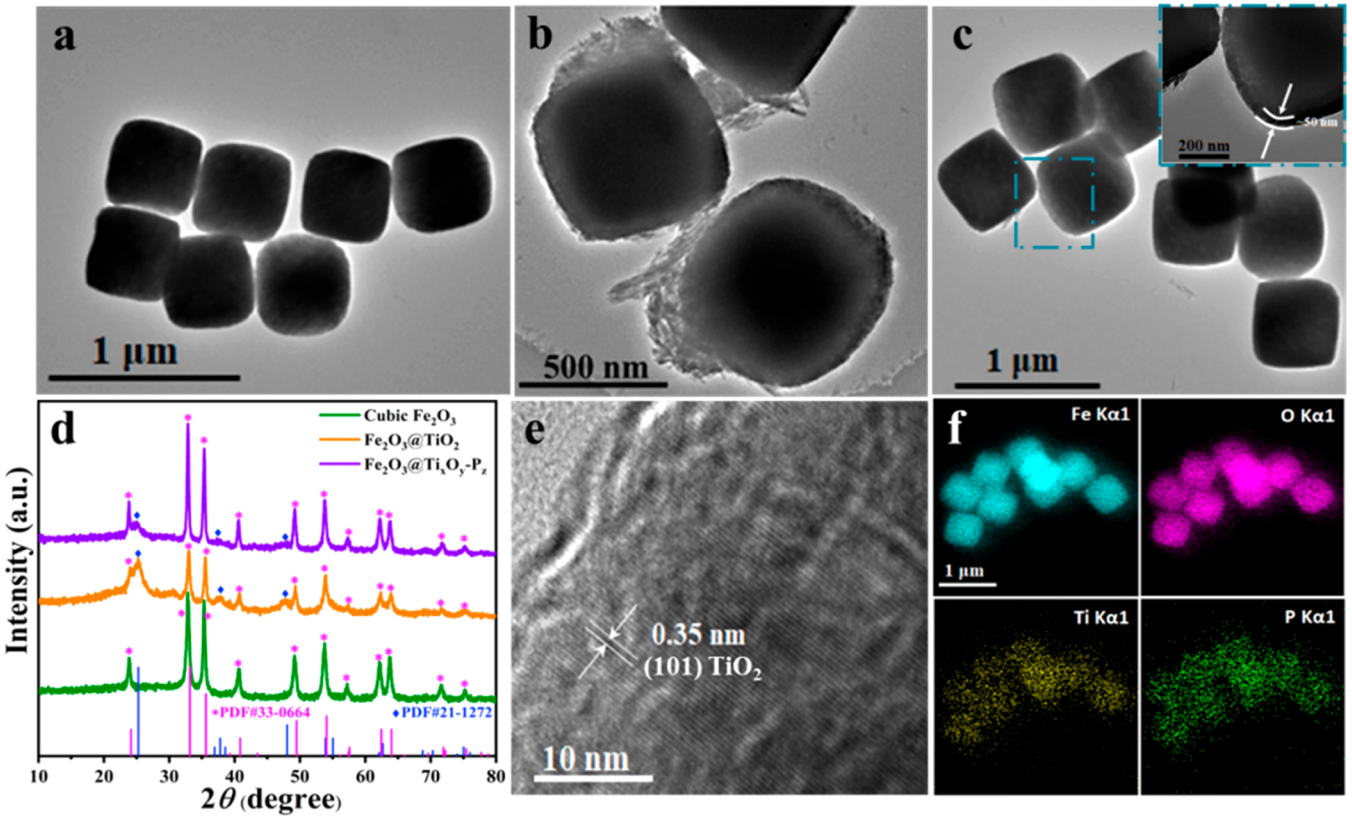

Figure 2. TEM imaging of cubic Fe_2O_3 (a), Fe_2O_3@TiO_2 (b), and Fe_2O_3@Ti_xO_y-P_z (c). The inset of part c is a higher resolution image of the dashed frame. XRD features (d) of as-synthesized cubic Fe_2O_3, Fe_2O_3@TiO_2, and Fe_2O_3@Ti_xO_y-P_z and standards α-Fe_2O_3 (Powder Diffraction File (PDF) 33-0664, International Centre for Diffraction Data (ICDD), 2004) and anatase TiO_2 (PDF 21-1272, ICDD, 2004; red lines). HRTEM image of Fe_2O_3@Ti_xO_y-P_z (e) and the EDS element mapping images of Fe, O, Ti, and P elements for Fe_2O_3@Ti_xO_y-P_z (f) from full-scale scans of part c.

alkaline hypochlorite liquor (A1727, Sigma-Aldrich) were afterward supplemented into 2.0 mL of the resulting solution. MS studies were carried out on an Agilent 1260-6460 (LC-MS).

Electrochemical Tests. The electrochemical test was completed via a CHI760-1 electro-chemistry workstation (Shanghai Chenhua, China) with a three-electrode cell. The glass-carbon electrode loaded catalyzer was the work electrode, and the saturated Ag/AgCl electrode and platinum foil were the reference electrode and anti-electrode, separately. The transient photocurrent response curves were harvested during the illumination (on/off) every 20 s at an applied potential of 0 V (vs Ag/AgCl) in 0.1 M Na_2SO_4 solution from the back side of the work electrode. The electrochemical impedance spectroscopy (EIS) measurements were completed by using an AC voltage amplitude of 5 mV in the frequency range between 105 and 0.01 Hz in 0.1 M Na_2SO_4 electrolyte under open circuit potential (OCP) conditions and 300 W xenon light irradiation. The Mott−Schottky (M−S) plots were implemented with the electrochemical window ranging between −0.5 and +0.7 V, using 800 Hz and an AC amplitude of 10 mV at each of the potentials.

N_2 Temperature-Programmed Desorption (N_2-TPD). A 100 mg portion of catalyzer was put in the U-shaped silica tube and preheated in Ar flow (50 mL min^{-1}) under 300 °C for 30 min and afterward cooled down to 25 °C. After pretreatment, the feed gas N_2 moved across the catalyzer bed under 25 °C for 1 h. After that, the removal of the physical adsorption of N_2 was realized by Ar flow (50 mL min^{-1}) under 50 °C for 48 min. In the end, the temperature of the catalyzer increased from 50 to 500 °C under 10 °C min^{-1}. We paid attention to various desorption species to determine the primary products produced from reactions of N_2 on catalyst and discovered that the sole species desorbed from the N_2-exposed samples is N_2, as analyzed online by a thermal conductivity detector (TCD, Micromeritics AutoChem II 2920).

RESULTS AND DISCUSSION

Morphology and Structure Properties of Fe_2O_3@Ti_xO_y-P_z. Figure 1a shows a schematic diagram about the formation mechanism regarding the Fe_2O_3@Ti_xO_y-P_z. First, a facile hydrothermal method was employed to synthesize cubic Fe_2O_3. Amorphous TiO_2 was deposited on the cubic Fe_2O_3 surfaces by the slow hydrolysis of titanium butoxide (TBOT). Finally, the Fe_2O_3@Ti_xO_y-P_z was obtained by annealing Fe_2O_3@TiO_2 with PH_3 under Ar flow, which generated abundant OVs and plenty of Ti^{3+} species on the layer of TiO_2. Hence, we obtained a disordered Ti_xO_y-P_z tier which covered the cubic Fe_2O_3 surface, and the layer had remarkable lattice deformation and plentiful oxygen defects and Ti^{3+} sites (for the detailed synthesis steps, see the Supporting Information). Subsequently, the content of TiO_2 loaded on cubic Fe_2O_3 was further optimized by using the PL spectral and photocurrent density as the basis. As shown in Figure S1, the Fe_2O_3@(0.6)-TiO_2 composite possesses the highest photocurrent density, which illustrated the enhancement of photogenerated electron−hole ability under visible light, which was beneficial to the improvement of photocatalytic performance. Therefore, the optimized catalyst of the Fe_2O_3@(0.6)TiO_2 composite was conducted for phosphating and denoted as Fe_2O_3@TiO_2 for the later experiments. Interestingly, in the process of doping, P atoms primarily replaced partial O and Ti to form O−Ti−P and O−P−O bonds, for reconstructing the surface of the TiO_2 layer with outstanding structure stability, improved electroconductibility, and good photocatalytic performance.

https://doi.org/10.1021/acssuschemeng.1c05890
ACS Sustainable Chem. Eng. XXXX, XXX, XXX−XXX

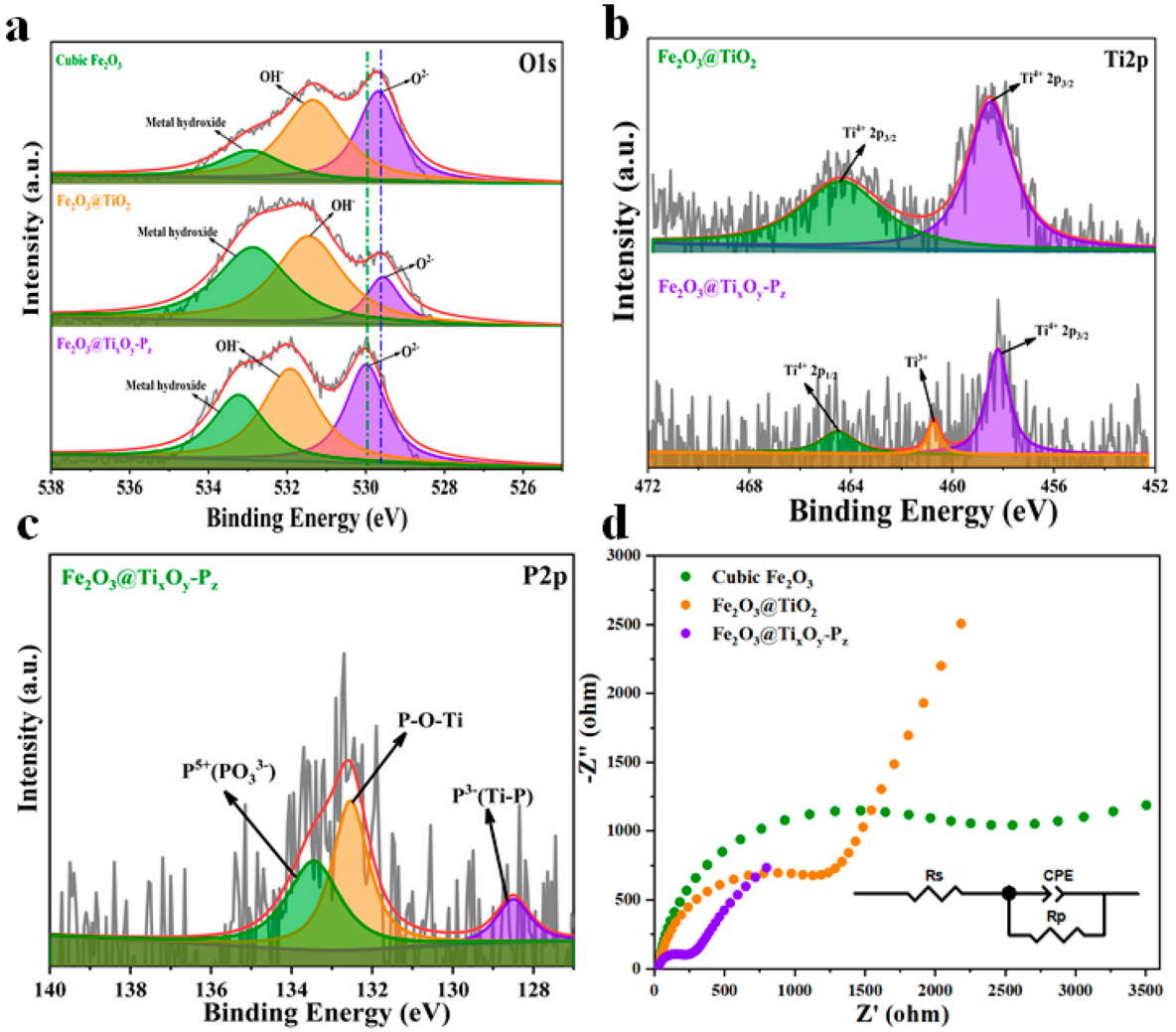

Figure 3. High-resolution XPS spectra of O 1s (a), Ti 2p (b), and P 2p (c) of cubic Fe_2O_3, Fe_2O_3@TiO_2, and Fe_2O_3@Ti_xO_y-P_z samples, as indicated. (d) Electrochemical impedance spectroscopy response for cubic Fe_2O_3, Fe_2O_3@TiO_2, and Fe_2O_3@Ti_xO_y-P_z samples in 0.1 M Na_2SO_4 aqueous solution, and the inset is the proposed equivalent circuit.

The morphology and structure of the cubic Fe_2O_3, Fe_2O_3@TiO_2, and Fe_2O_3@Ti_xO_y-P_z were identified via SEM. As presented by Figure 1b, for the cubic Fe_2O_3, the structure is highly uniform, and the size is ca. 547 nm. Figure 1c displays the SEM image about the core−shell Fe_2O_3@TiO_2, which demonstrates the triumphant covering of the amorphous TiO_2 phase over the cubic Fe_2O_3 surface. After treating with PH_3, the resulting Fe_2O_3@Ti_xO_y-P_z possessed a cube structure with an increased size of ca. 639 nm (Figure 1d). Figure 1e reveals that the Ti_xO_y-P_z layer thickness is approximately 50 nm. In addtion, the EDS line scan curves were used to further assess the morphological and structural status of the Fe_2O_3@Ti_xO_y-P_z. As depicted in Figure 1f and g, the content of P and Ti elements is less than Fe and O elements, and the P, Ti, and O elements first appear at both ends of the curve, while the Fe elements are distributed in the middle. This confirms that the core−shell structure of the designed photocatalyst of Fe_2O_3@Ti_xO_y-P_z has been successfully prepared.

The TEM, HRTEM, and EDS element mapping are in progress to identify and visualize the anatase TiO_2 phase coupled with the cubic Fe_2O_3. As shown in Figure 2a, the Fe_2O_3 has a cubic structure with uniform size. After hydrolysis of TiO_2, the cubic Fe_2O_3 surface had an amorphous layer with a random distribution (Figure 2b and Figure S4). After further phosphorization, there was a compact layer of which the thickness is ca. 50 nm on the Fe_2O_3 surface (inset of Figure 2c). The HRTEM image (Figure 2e) clearly demonstrates that the lattice spacing of the Fe_2O_3@Ti_xO_y-P_z is 0.35 nm with good crystallinity, which approximately matches the (101) diffraction facet of anatase TiO_2.[30,31] The element mapping characterizations assisted in further exploring the structure exhibited by the prepared Fe_2O_3@Ti_xO_y-P_z. Based on Figure 2f, the Fe, O, Ti, and P elements exhibit an identical distribution in the Fe_2O_3@Ti_xO_y-P_z, as shown in the STEM mapping (Figure 2c). Besides, the XRD features of the cubic Fe_2O_3, Fe_2O_3@TiO_2, and Fe_2O_3@Ti_xO_y-P_z nanocrystals are presented in Figure 2d. The standard PDFs regarding pure α-Fe_2O_3 (PDF 33-0664, ICDD, 2004; hematite, syn) and anatase TiO_2 (PDF 21-1272, ICDD, 2004; anatase, syn) served for the comparison. It is possible to index all of the positions and intensities about the α-Fe_2O_3 nanocrystals to standard PDFs, showing that α-Fe_2O_3 nanocrystals prepared here have a rhombohedral structure of hematite and the crystallinity is high. Following anatase TiO_2 coating, Fe_2O_3@TiO_2 composite nanocrystals saw obvious diffraction peaks regarding anatase TiO_2 and it is possible to index them to {101} (2θ = 25.28),

https://doi.org/10.1021/acssuschemeng.1c05890
ACS Sustainable Chem. Eng. XXXX, XXX, XXX−XXX

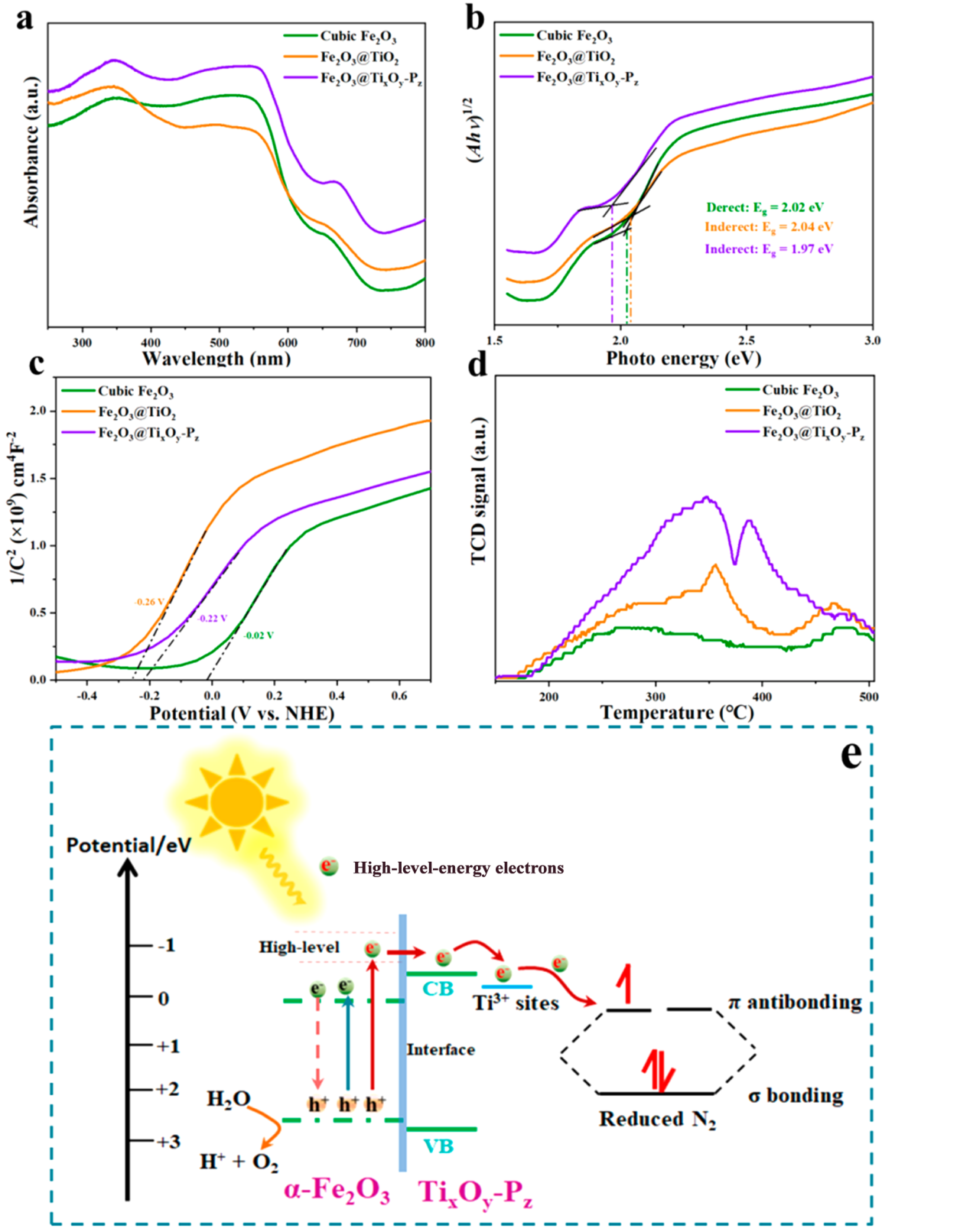

Figure 4. Role of the Ti^{3+} active sites induced by doping P atoms in the photoelectrochemical properties and electronic band structure of Fe_2O_3@Ti_xO_y-P_z. (a) UV−vis DRS of cubic Fe_2O_3, Fe_2O_3@TiO_2, and Fe_2O_3@Ti_xO_y-P_z. (b) The transformed Kubelka−Munk function of cubic Fe_2O_3, Fe_2O_3@TiO_2, and Fe_2O_3@Ti_xO_y-P_z for bandgap test from (a) UV−vis DRS plots. (c) M−S plots of cubic Fe_2O_3, Fe_2O_3@TiO_2, and Fe_2O_3@Ti_xO_y-P_z. (d) The N_2-TPD profiles for cubic Fe_2O_3, Fe_2O_3@TiO_2, and Fe_2O_3@Ti_xO_y-P_z. (e) Diagram of the aforementioned procedure for transference and space separation of light-driven HELEs in the fabricated Ti^{3+} defect-centered NRR mechanism on Fe_2O_3@Ti_xO_y-P_z.

{004} (2θ = 37.80), and {200} (2θ = 48.05) planes of anatase TiO_2 (Figure 2d). After annealing and phosphating, the diffraction peaks of Fe_2O_3@Ti_xO_y-P_z in Figure 2d are not conspicuous due to the stronger diffraction peaks of α-Fe_2O_3

https://doi.org/10.1021/acssuschemeng.1c05890
ACS Sustainable Chem. Eng. XXXX, XXX, XXX−XXX

relative to the Fe_2O_3@TiO_2 composite. The P-doped TiO_2 layer was a kind of polycrystalline material and could be submerged in the strong diffraction apex regarding monocrystalline α-Fe_2O_3 nanocrystals (Figure 2d, curve of Fe_2O_3@Ti_xO_y-P_z).[32,33]

Moreover, high-resolution XPS spectra regarding O 1s and Ti 2p were interrogated specially to evaluate the presence of Ti^{3+} species. As presented by the high-resolution XPS spectra regarding O 1s (Figure 3a, curve of cubic α-Fe_2O_3 and Fe_2O_3@TiO_2), the peaks at 529.6, 531.4, and 532.9 eV indicated that there were three types of oxygen species, assigned as O^{2-} (Fe−O bond or Ti−O bond), surface-adsorbed oxygen species (OH^-), and metal hydroxide, respectively.[34,35] As displayed in the curve of Fe_2O_3@Ti_xO_y-P_z (Figure 3b), an overt shift of O 1s toward higher binding energy implies the presence of Ti^{3+} species and OVs.[28,30] In high-resolution XPS spectra regarding Ti 2p, two peaks were discovered at 458.50 eV (Ti $2p_{3/2}$) and 464.37 eV (Ti $2p_{1/2}$), and can be assigned to Ti^{4+} states (Figure 3b, curve of Fe_2O_3@TiO_2). For the Fe_2O_3@Ti_xO_y-P_z sample, a new peak appeared at 460.73 eV, which could be assigned to the Ti^{3+} species, showing that Ti^{3+} species were formed following the phosphorization.[36] The Ti^{3+} level was further analyzed by double integral of EPR spectra quantitatively (Figure S9a,b).[28,37] The Ti^{3+} defect concentration of the as-synthesized Fe_2O_3@Ti_xO_y-P_z sample was speculated as 4.61 μmol g^{-1} by treatment with 1.0 g of NaH_2PO_2. Moreover, the level of Ti^{3+} species presents a progressive elevation trend with the rise of NaH_2PO_2 amount (Figure S9c,d), revealing that the treatment of NaH_2PO_2 could effectively induce the production of Ti^{3+} species. Such a tunable Ti^{3+} defect strategy provides a new idea for the development of excellent photocatalytic N_2 reduction catalysts in the future.

For obtaining more evidence, the P states were examined by high-resolution XPS spectra of P 2p. Figure 3c displays the P 2p XPS spectra regarding Fe_2O_3@Ti_xO_y-P_z, and a marked peak can be found at 132.54 eV, confirming the existence of a P−O−Ti bond in the annealed Fe_2O_3@Ti_xO_y-P_z. Meanwhile, the peak at 133.45 eV could be due to the pentavalent oxidation states (P^{5+}).[38] Referring to previous reports, P atoms might be introduced as cations (P^{5+}) and substituted for Ti^{4+} ions in the prepared TiO_2 samples by P-doped, like S^{6+} [39,40] and I^{5+}[41] doped TiO_2. The existence of a P−O−Ti bond and doping of P^{5+} is conducive to the formation of an excellent structure and a stable TiO_2 layer.[42] Besides, peaks at 128.50 eV were also found, which corresponds to the Ti−P bond (P^{3-} states). The P^{3-} substitutes for O atoms in the TiO_2 crystal lattice, inducing the production of Ti^{3+} active sites, which could be because the electrons of P^{3-} tend to transfer to the nearby Ti^{4+} ions. Meanwhile, the actual P content in the Fe_2O_3@Ti_xO_y-P_z sample is obtained through inductively coupled plasma optical emission spectroscopy (ICP-OES) measurements (listed in Table S1). As shown in Figure 3d, the semicircular radius of Fe_2O_3@Ti_xO_y-P_z in the high-frequency area is smaller in contrast to Fe_2O_3@TiO_2 and cubic Fe_2O_3, indicating that Fe_2O_3@Ti_xO_y-P_z has a lower charge transference resistance and a greater charge transfer rate.[43] Such a phenomenon might be due to the close interface contacts between the Ti_xO_y-P_z layer and Fe_2O_3, which could provide the valid channel for electron transference. Interestingly, after modification of P in TiO_2, a layer containing Ti^{3+} active sites with excellent structure, enhanced electronic conductivity, and high stability was successfully constructed.

Ti^{3+} and Its Roles on Fe_2O_3@Ti_xO_y-P_z. The presence of Ti^{3+} species remarkably affects the pNRR properties of the TiO_2-based materials.[27,44] UV−vis diffuse reflectance spectroscopy (UV−vis DRS) shows that the individual cubic Fe_2O_3 has a better visible light response (Figure 4a, curve of cubic Fe_2O_3). After recombination with TiO_2, the visible light response decreases, whereas the UV light response is enhanced (Figure 4a, curve of Fe_2O_3@TiO_2). Eventually, in the visible region, with PH_3-treated, the spectrum of Fe_2O_3@Ti_xO_y-P_z presents a strong absorption response, mainly because the Ti^{3+} sites exist on the Ti_xO_y-P_z surface (Figure 4a, curve of Fe_2O_3@Ti_xO_y-P_z).[45] Through Kubelka−Munk transformation (Figure 4b) from UV−vis DRS (Figure 4a), the direct band gap value of cubic Fe_2O_3 is speculated as 2.02 eV, and the indirect band gap values of Fe_2O_3@TiO_2 and Fe_2O_3@Ti_xO_y-P_z are 2.04 and 1.97 eV vs NHE, separately. Meanwhile, the Mott−Schottky is a typical approach to label the flat band of the semiconductor, and the conduction bands of cubic Fe_2O_3, Fe_2O_3@TiO_2, and Fe_2O_3@Ti_xO_y-P_z are tested to be −0.02, −0.26< and −0.22 eV, respectively (Figure 4c). Then, the valence band potential can be derived from the values between bandgap and conduction band and are calculated to be 2.00, 1.78, and 1.75 eV vs NHE. Therefore, coupling of a wide bandgap of TiO_2 with α-Fe_2O_3 forms a more negative conduction band potential architecture which is thermodynamically beneficial for the pNRR of reactants. The introduction of Ti^{3+} species on Fe_2O_3@Ti_xO_y-P_z may lead to the creation of a new energy level because Ti^{3+} self-doping presents below the conduction band; as a result, a strong response is generated in the visible region and the inherent bandgap is narrowed (Figure 4a−c).

The effective N_2 chemisorption toward catalyst plays a pivotal role in the solar N_2 fixation process, and it is commonly believed that the process occurs at the catalytic active sites as a crucial step specific to pNRR.[46] The N_2 temperature-programmed desorption (N_2-TPD) was employed for measuring the ability of the catalysts to adsorb N_2. Generally, when the catalytic material has a higher N_2-TPD peak, it means that the pNRR activity is higher.[47] As shown in Figure 4d, for the Fe_2O_3@Ti_xO_y-P_z, the N_2 desorption peak is much stronger compared with cubic Fe_2O_3 and Fe_2O_3@TiO_2 at 250−450 °C, basically relying on the N_2 chemisorption capacity of the samples under room temperature. This data indicates that the PH_3-induced Ti^{3+} sites of Fe_2O_3@Ti_xO_y-P_z could offer a large amount of chemical adsorption sites for capturing N_2 from water. As the N_2 adsorption is the first step for NH_3 synthesis, the favorable N_2 absorption on Fe_2O_3@Ti_xO_y-P_z is beneficial for the whole pNRR process.[25]

Combined with the previously reported Fe_2O_3−TiO_2 wide−narrow band gap photocatalysis system,[20,32,48] the electronic energy-level diagram about Fe_2O_3@Ti_xO_y-P_z was constructed (Figure 4e). Obviously, VB-to-CB excitation of the photogenerated electrons is possible regarding cubic α-Fe_2O_3 in various energy levels under light irradiation, including the high-energy region and low-energy region in the system.[49] On the one hand, the photogenerated electrons in the low-energy region, after rapidly relaxing to the VB bottom of α-Fe_2O_3, can be recombined with holes. On the other hand, partial HELEs would experience a thermodynamical transfer to the CB of TiO_2;[50,51] consequently, the lifetime would be prolonged and charge carriers would be separated more easily. That is, the excited HELEs of α-Fe_2O_3 capable of overcoming the restriction can be further transferred to the CB of Ti_xO_y-P_z; then, they are trapped by the Ti^{3+} sites and injected into the

https://doi.org/10.1021/acssuschemeng.1c05890
ACS Sustainable Chem. Eng. XXXX, XXX, XXX−XXX

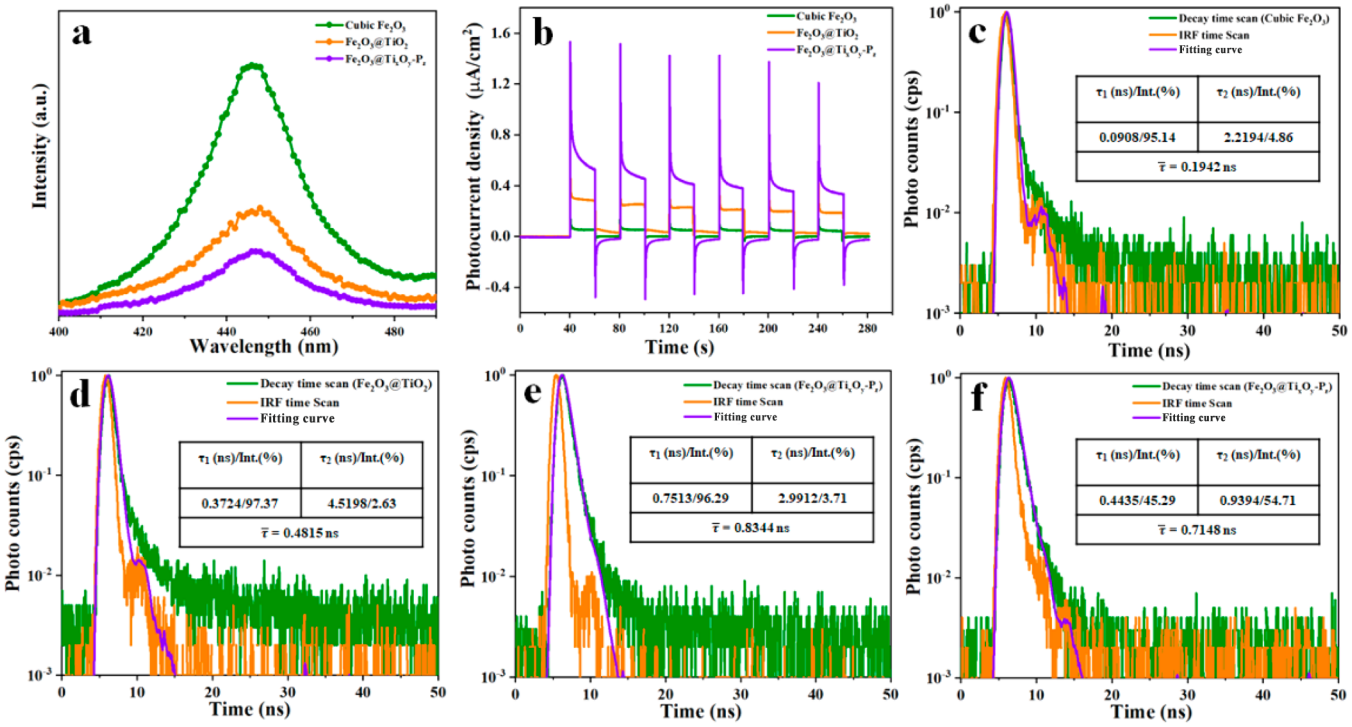

Figure 5. PL spectra (a) and transient photocurrent response (b) of cubic Fe_2O_3, Fe_2O_3@TiO_2, and Fe_2O_3@Ti_xO_y-P_z. Time-resolved PL decay spectra of cubic Fe_2O_3 (c), Fe_2O_3@TiO_2 (d), and Fe_2O_3@Ti_xO_y-P_z (e) under an Ar atmosphere. Time-resolved fluorescence decay spectra of Fe_2O_3@Ti_xO_y-P_z (f) under a N_2 atmosphere.

antibond orbital (π^*) of adsorbed N_2; hence, the N_2 activation and the N≡N triple bond cleavage are enhanced.[25,26,52] The pNRR activity of the well-designed Fe_2O_3@Ti_xO_y-P_z composites is enhanced owing to the two semiconductors that experience rapid interfacial charge transfer. The ultimate goal of improving pNRR abilities lies in effectively separating the electron−hole pairs.

We conducted the photoluminescence (PL) measurement to further explore the kinetic behaviors related to carriers, detecting the PL signal of the samples by a 350 nm excited light (Figure 5a). Relative to the obvious emission peaks for cubic Fe_2O_3 and Fe_2O_3@TiO_2, Fe_2O_3@Ti_xO_y-P_z displays a weaker PL peak, which demonstrates that the Fe_2O_3@Ti_xO_y-P_z possesses a smaller recombination velocity of electrons and holes. We further explored the migration, transfer, and recombination of electron−hole pairs using photocurrent, under the irradiation of a 300 W xenon lamp. As shown in Figure 5b, samples present a rapid light current response to the periodic light on−off. Fe_2O_3@Ti_xO_y-P_z presents a significantly higher photocurrent intensity relative to cubic Fe_2O_3 and Fe_2O_3@TiO_2, verifying the better condition for carrier separation in Fe_2O_3@Ti_xO_y-P_z. That mainly benefits from the coated Ti_xO_y-P_z layer on the cubic Fe_2O_3 surface; as a result, impurity levels and carrier trapping centers are formed, thereby facilitating photoinduced electrons and holes to separate and suppressing the recombination.[28]

Most importantly, as corroborative evidence for the above process (Figure 4e), the time-resolved PL decay served for identifying enriched photoinduced electron injection from the Ti^{3+} sites to N_2 (Figure 5c−f). The Fe_2O_3@Ti_xO_y-P_z presents a strikingly slower decay kinetics compared with the cubic Fe_2O_3 and Fe_2O_3@TiO_2, and the charge carriers of the Fe_2O_3@Ti_xO_y-P_z have a decay lifetime of 0.8344 ns (Figure 5e), significantly longer than 0.4815 ns for Fe_2O_3@TiO_2 (Figure 5d) and 0.1942 ns for the cubic Fe_2O_3 (Figure 5c) under an Ar atmosphere. It can be found that the charge carrier recombination in the Fe_2O_3@Ti_xO_y-P_z could be effectively inhibited. Moreover, the Fe_2O_3@Ti_xO_y-P_z average decay time in the N_2 atmosphere presented an obvious decrease from 0.8344 to 0.7148 ns after creating Ti^{3+} species (Figure 5f), strongly demonstrating the direct injection of Ti^{3+}-site-trapped photogenerated electrons into chemically adsorbed N_2 and the following quenching.[47,51]

NRR Activity of Fe_2O_3@Ti_xO_y-P_z. Indophenol reagent colorimetry served for evaluating the performance of photocatalytic N_2 fixation exhibited by Fe_2O_3@Ti_xO_y-P_z with Ti^{3+} active sites, and in the process, water molecules were taken as the solvent for providing protons under a full spectrum (Figure 6a, Figure S3). To explore the reasons for the improvement of pNRR activity of the Fe_2O_3@Ti_xO_y-P_z composites, we specially prepared the PH_3 treatment of the pristine cubic Fe_2O_3 (denoted as Fe_2O_3-P_z) and the single defective Ti_xO_y-P_z layer (see Figure S5 and Figure S6). As presented by Figure 6a, almost no NH_3 was identified with N_2 in the dark. With experiments proceeding under light irradiation, the photocatalytic NH_3 production rate of all of the catalysts exhibited a gradual enhancement with increasing time in the N_2 atmosphere. After 180 min, a small amount of NH_3 was obtained in the case of cubic Fe_2O_3 or Fe_2O_3-P_z in the atmosphere of N_2, while a significant amount of NH_3 generated obviously based on the catalysts of Fe_2O_3@Ti_xO_y-P_z. As demonstrated in Figure 6b, it was calculated that the pNRR rate driven by full-spectrum light was estimated to be 1.87 μmol $g_{cat.}^{-1}$ h^{-1} for Fe_2O_3-P_z, which is just 1.13 times of cubic Fe_2O_3 (1.66 μmol $g_{cat.}^{-1}h^{-1}$). Although the single Ti_xO_y-P_z layer possessed a relatively high pNRR activity, it was still not comparable to that of Fe_2O_3@Ti_xO_y-P_z composites (15.65 μmol $g_{cat.}^{-1}$ h^{-1}). This conspicuous pNRR rate based on

https://doi.org/10.1021/acssuschemeng.1c05890
ACS Sustainable Chem. Eng. XXXX, XXX, XXX−XXX

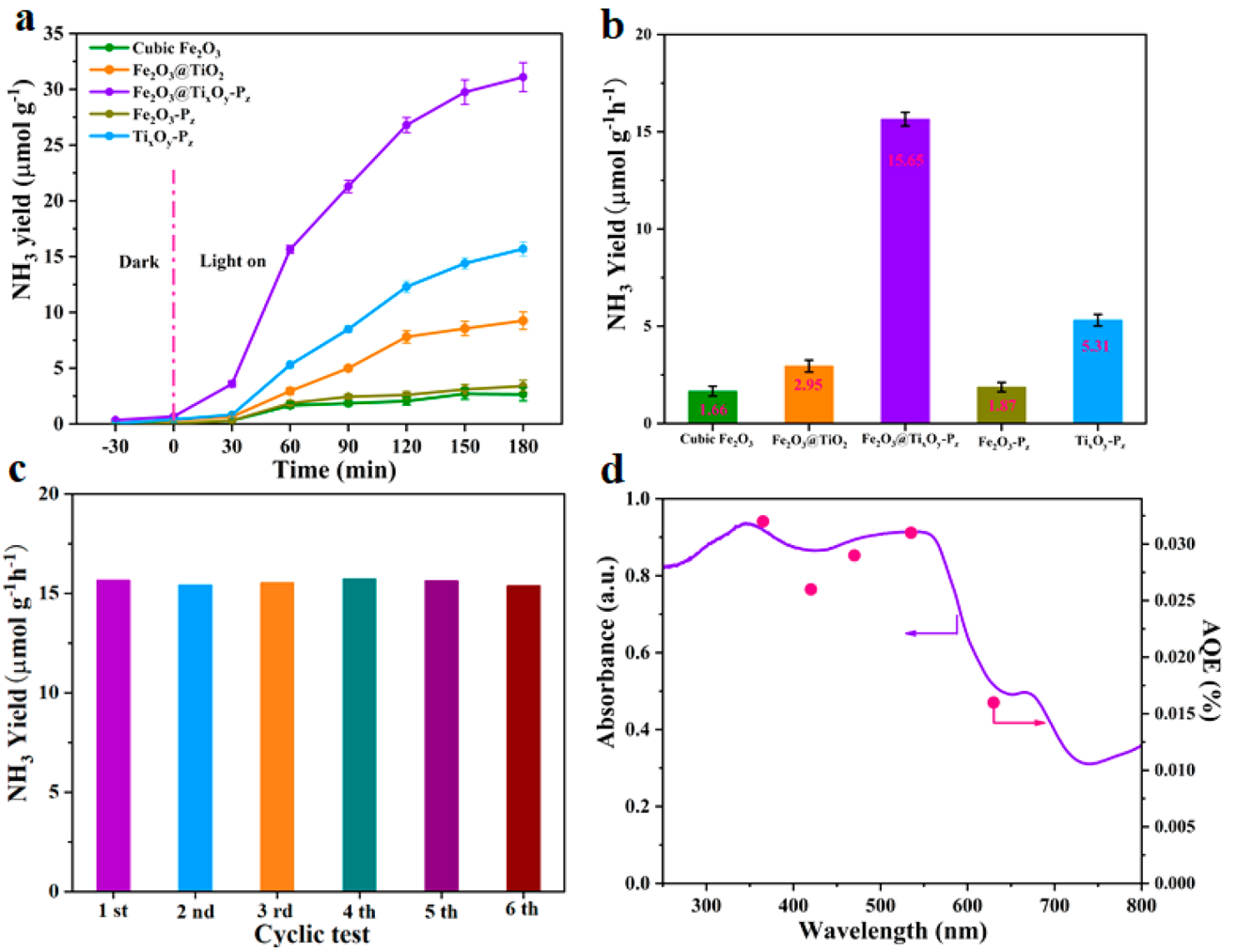

Figure 6. Catalysis surveys for light-induced N_2 fixing via a variety of catalyzers. (a) Quantitation measurement of the produced NH_3 by full spectra illumination with an indophenol indicator over different systems in N_2. (b) Photocatalytic NH_3 production rate of cubic Fe_2O_3, Fe_2O_3@TiO_2, Fe_2O_3@Ti_xO_y-P_z, Fe_2O_3-P_z, and Ti_xO_y-P_z in the first 1 h. (c) Photocatalytic cycling tests for Fe_2O_3@Ti_xO_y-P_z. (d) Wavelength-dependent apparent quantum efficiency of the as-synthesized Fe_2O_3@Ti_xO_y-P_z with monochromatic illumination.

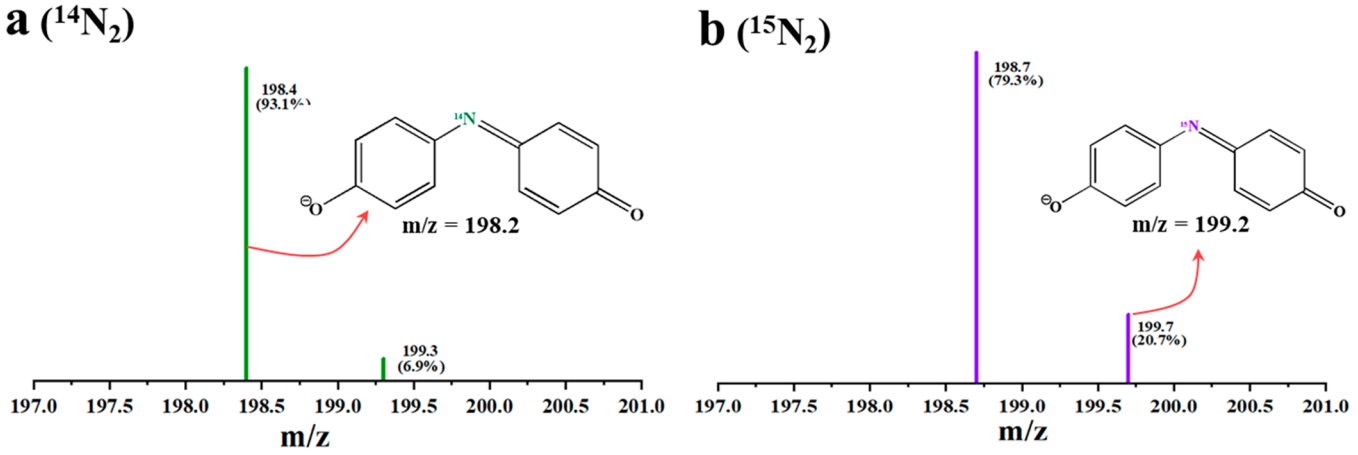

Figure 7. Mass spectral illustrations of the indophenol from diverse atmospheric conditions. (a) The mass spectral illustrations of the indophenol prepared from $^{14}N_2$ atmospheric conditions. (b) The mass spectra of the indophenol prepared from $^{15}N_2$ atmospheric conditions.

Fe_2O_3@Ti_xO_y-P_z composites is dramatically higher than those of the other catalysts and was also prominent among the reported literature (Figure 6b, Table S2). These data indicated that the coupled TiO_2 or single defective Ti_xO_y-P_z layer could greatly boost the pNRR activity of Fe_2O_3. By virtue of the efficient separation of photogenerated charges and the improvement of surface active sites, the Fe_2O_3@Ti_xO_y-P_z possesses an excellent pNRR activity.

https://doi.org/10.1021/acssuschemeng.1c05890
ACS Sustainable Chem. Eng. XXXX, XXX, XXX−XXX

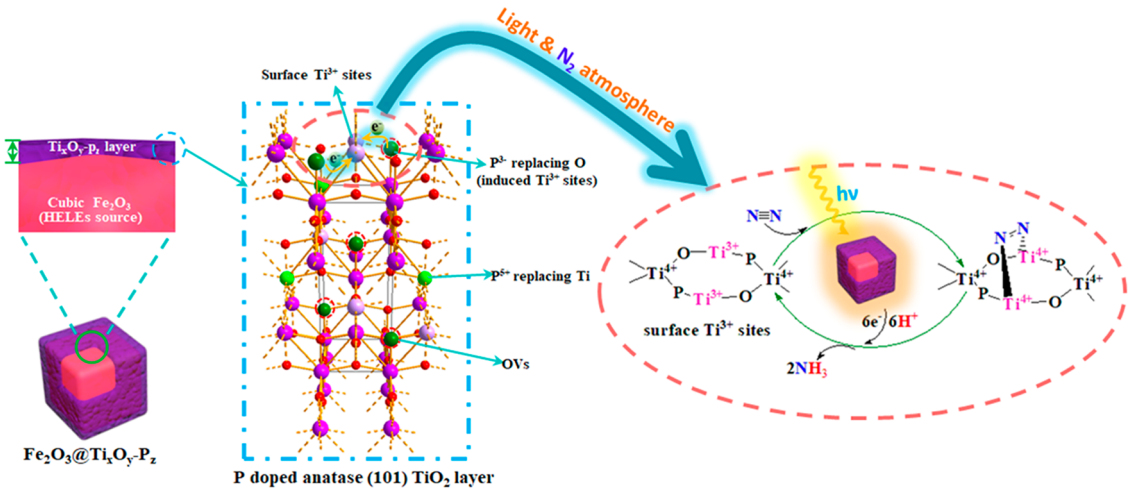

Figure 8. Diagram of the possible formation mechanism of stable Ti^{3+} sites in the anatase (101) TiO_2 layer on cubic Fe_2O_3 and the proposed mechanism for photocatalytic fixation of N_2 over the surface of $Fe_2O_3@Ti_xO_y$-P_z.

In addition, the $Fe_2O_3@Ti_xO_y$-P_z possesses structural stability and photocatalytic stability, as proved by an insignificant variation in activities, morphological status, or physico-chemistry performances after pNRR 6 cycle experiments (Figure 6c, Figure S7, and Figure S8). For measuring the apparent quantum efficiency (AQE) related to pNRR over $Fe_2O_3@Ti_xO_y$-P_z, experiments regarding the photocatalytic N_2 reduction were conducted under various monochromatic light irradiations (365, 420, 470, 535, and 630 nm) (Figure 6d; for detailed information, see the Supporting Information). The associated AQE values of $Fe_2O_3@Ti_xO_y$-P_z are 0.032, 0.026, 0.029, 0.031, and 0.016%, respectively, for the monochromatic light wavelength increasing from 365 to 630 nm, that followed the absorption edge about the $Fe_2O_3@Ti_xO_y$-P_z semiconductor, possessing acceptable utilization of solar energy (Figure 6d).

For verifying whether photocatalytic N_2 fixation on the $Fe_2O_3@Ti_xO_y$-P_z was authentic, we conducted photocatalytic N_2 fixation under ^{15}N isotope-labeled N_2 (with the purity not less than 99%). The produced $^{15}NH_4^+$ can react with phenol and hypochlorite for the formation of ^{15}N-labeled indophenol,[53,54] which was assayed by LC-MS. Figure 7a displays a potent mass spectroscopy signal of ^{14}N-labeled indophenol anion at about 198.4 m/z in LC-MS research when using $^{14}N_2$ as the feeding gas. Notably, ^{15}N-labeled indophenol negative ion showed a significantly reinforced mass spectrum signal at about 199.7 m/z in LC-MS studies (Figure 7b). The signal had a higher intensity relative to the ^{14}N:^{15}N natural abundance ratio after 30 min of light radiation. Besides, the time-dependent tests were conducted by utilizing $^{15}N_2$ as the feed gas. As shown in Figure S10, the signal intensity of the ^{14}N:^{15}N natural abundance ratio from indophenol anion increased significantly with the increase of light radiation time. That further identified N_2 as the source to generate ammonium ion in the experiment.

Proposed Catalytic Mechanism of $Fe_2O_3@Ti_xO_y$-P_z for pNRR. Based on the aforementioned discussions, the proposed catalytic mechanism of $Fe_2O_3@Ti_xO_y$-P_z for pNRR could be described in Figure 8. The Ti^{3+} species were drawn into the anatase (101) TiO_2 layer by PH_3 treatment on the cubic Fe_2O_3 and behaved as active sites for pNRR. The complex excellent structure of the Ti_xO_y-P_z layer containing Ti^{3+} sites, OVs, titanium metal defects, and doped P atoms with different valence states led to an excellent structural stability, high conductivity, and efficient photocatalytic performance, which indicates that the highly active Ti_xO_y-P_z layer could not only serve as a HELE receiving platform of narrow band gap α-Fe_2O_3 but also significantly improve its pNRR performance. Under the solar light irradiation, cubic Fe_2O_3 plays the role of the core component of photocatalyst and will be capable of absorbing solar energy as well as generating partial HELEs transferred to the Ti_xO_y-P_z layer, which then are trapped by the Ti^{3+} active sites and injected into the antibond orbital (π^*) of the adsorbed N_2; hence, the N≡N triple bond will be activated efficiently. In this case, it will continue to be weakened by Ti^{3+} active sites together with hydrogenation before the N≡N triple bond cleavage to NH_3 at last.

CONCLUSION

In summary, the photocatalytic activity of α-Fe_2O_3 driven by sunlight for N_2 fixation is greatly boosted after coupling the Ti_xO_y-P_z layer. The reinforced activity is due to the evident elevation in the lifetime and separation of photogenerated charges through transference of the HELEs of α-Fe_2O_3 to the Ti_xO_y-P_z layer. It is confirmed that the Ti_xO_y-P_z layer has a trifunctional effect and serves as an appropriate platform for the acceptance of more HELEs because of its proper CB position, providing sufficient Ti^{3+} active sites for pNRR, and doped P atoms makes the whole catalyst with defective sites highly stable. Moreover, as verified by isotopic experiments, the synthesized NH_3 fully originated from the N_2 supply. According to TPD and time-resolved PL decay spectra, the Ti^{3+} centers of $Fe_2O_3@Ti_xO_y$-P_z serve as active sites for the N_2 chemisorption and N≡N triple bond cleavage. Therefore, $Fe_2O_3@Ti_xO_y$-P_z displays a remarkable NH_3 generation amount of 15.65 μmol $g_{cat.}^{-1}$ h^{-1}, which is 9.43, 5.31, 8.37, and 2.95 times higher than cubic Fe_2O_3, $Fe_2O_3@TiO_2$, Fe_2O_3-P_z, and Ti_xO_y-P_z. It is expected that the strategy can serve for the development of other highly efficient precious metal free defective photocatalysts for creating N_2 reduction with high activity under ambient conditions.

https://doi.org/10.1021/acssuschemeng.1c05890
ACS Sustainable Chem. Eng. XXXX, XXX, XXX−XXX

■ ASSOCIATED CONTENT

Supporting Information

The Supporting Information is available free of charge at https://pubs.acs.org/doi/10.1021/acssuschemeng.1c05890.

Additional experimental details, materials, and methods, including the preparation of cubic Fe_2O_3, Fe_2O_3@TiO_2, Fe_2O_3@Ti_xO_y-P_z, Fe_2O_3-P_z, and the hollow Ti_xO_y-P_z nanolayer, the optimization of Fe_2O_3@TiO_2 composites, determination of apparent quantum efficiency (AQE), and determination of Ti^{3+} defect concentration; photographs of the experimental setup, characterization data, and evaluation of photocatalyt performance including Figures S1−S10 and Tables S1 and S2 (PDF)

■ AUTHOR INFORMATION

Corresponding Authors

Dongxue Han − *School of Civil Engineering c/o Center for Advanced Analytical Science, Guangzhou Key Laboratory of Sensing Materials & Devices, School of Chemistry and Chemical Engineering, Guangzhou Higher Education Mega Center, Guangzhou University, Guangzhou 510006, P. R. China; University of Chinese Academy of Sciences, Beijing 100049, P. R. China;* orcid.org/0000-0002-7343-2221; Email: dxhan@gzhu.edu.cn

Ying He − *School of Civil Engineering c/o Center for Advanced Analytical Science, Guangzhou Key Laboratory of Sensing Materials & Devices, School of Chemistry and Chemical Engineering, Guangzhou Higher Education Mega Center, Guangzhou University, Guangzhou 510006, P. R. China*; Email: ccyhe@gzhu.edu.cn

Authors

Wensheng Zhang − *School of Civil Engineering c/o Center for Advanced Analytical Science, Guangzhou Key Laboratory of Sensing Materials & Devices, School of Chemistry and Chemical Engineering, Guangzhou Higher Education Mega Center, Guangzhou University, Guangzhou 510006, P. R. China*

Dongfang Han − *School of Civil Engineering c/o Center for Advanced Analytical Science, Guangzhou Key Laboratory of Sensing Materials & Devices, School of Chemistry and Chemical Engineering, Guangzhou Higher Education Mega Center, Guangzhou University, Guangzhou 510006, P. R. China*

Mengjiao Dai − *State Key Laboratory of Electroanalytical Chemistry, c/o Engineering Laboratory for Modern Analytical Techniques, Changchun Institute of Applied Chemistry, Chinese Academy of Sciences, Changchun 130022, P. R. China; University of Chinese Academy of Sciences, Beijing 100049, P. R. China*

Yingying Fan − *School of Civil Engineering c/o Center for Advanced Analytical Science, Guangzhou Key Laboratory of Sensing Materials & Devices, School of Chemistry and Chemical Engineering, Guangzhou Higher Education Mega Center, Guangzhou University, Guangzhou 510006, P. R. China*

Guoliang Pan − *School of Civil Engineering c/o Center for Advanced Analytical Science, Guangzhou Key Laboratory of Sensing Materials & Devices, School of Chemistry and Chemical Engineering, Guangzhou Higher Education Mega Center, Guangzhou University, Guangzhou 510006, P. R. China*

Weiqi Liang − *School of Civil Engineering c/o Center for Advanced Analytical Science, Guangzhou Key Laboratory of Sensing Materials & Devices, School of Chemistry and Chemical Engineering, Guangzhou Higher Education Mega Center, Guangzhou University, Guangzhou 510006, P. R. China*

Qitong Zheng − *School of Civil Engineering c/o Center for Advanced Analytical Science, Guangzhou Key Laboratory of Sensing Materials & Devices, School of Chemistry and Chemical Engineering, Guangzhou Higher Education Mega Center, Guangzhou University, Guangzhou 510006, P. R. China*

Dongdong Qin − *School of Civil Engineering c/o Center for Advanced Analytical Science, Guangzhou Key Laboratory of Sensing Materials & Devices, School of Chemistry and Chemical Engineering, Guangzhou Higher Education Mega Center, Guangzhou University, Guangzhou 510006, P. R. China*

Li Niu − *School of Civil Engineering c/o Center for Advanced Analytical Science, Guangzhou Key Laboratory of Sensing Materials & Devices, School of Chemistry and Chemical Engineering, Guangzhou Higher Education Mega Center, Guangzhou University, Guangzhou 510006, P. R. China; University of Chinese Academy of Sciences, Beijing 100049, P. R. China;* orcid.org/0000-0003-3652-2903

Complete contact information is available at: https://pubs.acs.org/10.1021/acssuschemeng.1c05890

Author Contributions

The manuscript was written through contributions of all authors. All authors have given approval to the final version of the manuscript.

Notes

The authors declare no competing financial interest.

■ ACKNOWLEDGMENTS

This work was sponsored by the National Natural Science Foundation of China (22172040, 21974031), the Department of Science and Techniques of Guangdong Province (2021A1515010180, 2019B010933001), Guangzhou Municipal Science and Technology Bureau (202102010449), and the Department of Guangdong Provincial Public Security (GZQC20-PZ11-FD084). We would like to thank Shiyanjia Lab platform (www.shiyanjia.com) for providing XPS and TPD experimental testing and analysis services.

■ REFERENCES

(1) Smil, V. Detonator of the Population Explosion. *Nature* **1999**, *400*, 415.

(2) Zhao, Y.; Zhao, Y.; Shi, R.; Wang, B.; Waterhouse, G. I. N.; Wu, L. Z. Tuning oxygen vacancies in ultrathin TiO_2 nanosheets to boost photocatalytic nitrogen fixation up to 700 nm. *Adv. Mater.* **2019**, *31*, 1806482.1−1806482.9.

(3) Service, R. F. New recipe produces ammonia from air, water, and sunlight. *Science* **2014**, *345*, 610−610.

(4) Lan, R.; Tao, S. Ammonia as a Suitable Fuel for Fuel Cells. *Front. Energy Res.* **2014**, *2*, 1−4.

(5) Shiraishi, Y.; Shiota, S.; Kofuji, Y.; Hashimoto, M.; Chishiro, K.; Hirakawa, H.; Tanaka, S.; Ichikawa, S.; Hirai, T. Nitrogen fixation with water on carbon-nitride-based metal-free photocatalysts with 0.1% solar-to-ammonia energy conversion efficiency. *ACS Appl. Energy Mater.* **2018**, *1*, 4169−4177.

(6) Xie, X. Y.; Xiao, P.; Fang, W. H.; Cui, G.; Thiel, W. Probing photocatalytic nitrogen reduction to ammonia with water on the rutile

TiO_2 (110) surface by first-principles calculations. *ACS Catal.* **2019**, *9* (10), 9178−9187.
(7) Chen, J. G.; Crooks, R. M.; Seefeldt, L. C.; Bren, K. L.; Bullock, R. M.; Darensbourg, M. Y.; Holland, P. L.; Hoffman, B.; Janik, M. J.; Jones, A. K.; Kanatzidis, M. G.; King, P.; Lancaster, K. M.; Lymar, S. V.; Pfromm, P.; Schneider, W. F.; Schrock, R. R. Beyond Fossil FuelDriven Nitrogen Transformations. *Science* **2018**, *360*, No. eaar6611.
(8) Kyriakou, V.; Garagounis, I.; Vasileiou, E.; Vourros, A.; Stoukides, M. Progress in the electrochemical synthesis of ammonia. *Catal. Today* **2017**, *286*, 2−13.
(9) Zhang, S.; Zhao, Y. X.; Shi, R.; Waterhouse, G. I. N.; Zhang, T. R. Photocatalytic ammonia synthesis: Recent progress and future. *EnergyChem.* **2019**, *1*, 100013.
(10) Bagger, A.; Wan, H.; Stephens Ifan, E. L.; Rossmeisl, J. Role of Catalyst in Controlling N_2 Reduction Selectivity: A Unified View of Nitrogenase and Solid Electrodes. *ACS Catal.* **2021**, *11*, 6596−6601.
(11) Wang, J.; Nan, H. F.; Tian, Y.; Chu, K. $FeMo_3S_4$ for Efficient Nitrogen Reduction Reaction. *ACS Sustainable Chem. Eng.* **2020**, *8* (34), 12733−12740.
(12) Zhang, S.; Zhao, Y. X.; Shi, R.; Zhou, C.; Waterhouse Geoffrey, I. N.; Wang, Z.; Weng, Y. X.; Zhang, T. R. Sub-3 nm Ultrafine Cu_2O for Visible Light-driven Nitrogen Fixation. *Angew. Chem., Int. Ed.* **2021**, *60*, 2554.
(13) Bo, Y. N.; Wang, H. Y.; Lin, Y. X.; Yang, T.; Ye, R.; Li, Y.; Hu, C. Y.; Du, P. Y.; Hu, Y. G.; Liu, Z.; Long, R.; Gao, C.; Ye, B. J.; Song, L.; Wu, X. J.; Xiong, Y. J. Altering Hydrogenation Pathways in Photocatalytic Nitrogen Fixation by Tuning Local Electronic Structure of Oxygen Vacancy with Dopant. *Angew. Chem., Int. Ed.* **2021**, *60*, 16085.
(14) Maeda, K.; Domen, K. New Non-Oxide Photocatalysts Designed for Overall Water Splitting under Visible Light. *J. Phys. Chem. C* **2007**, *111*, 7851−7861.
(15) Barreca, D.; Carraro, G.; Gasparotto, A.; Maccato, C.; Sada, C.; Singh, A. P.; Mathur, S.; Mettenbçrger, A.; Bontempi, E.; Depero, L. E. Columnar Fe_2O_3 arrays via plasma-enhanced growth: Interplay of fluorine substitution and photoelectrochemical properties. *Int. J. Hydrogen Energy* **2013**, *38*, 14189−14199.
(16) Carraro, G.; Maccato, C.; Gasparotto, A.; Montini, T.; Turner, S.; Lebedev, O. I.; Gombac, V.; Adami, G.; Tendeloo, G. V.; Barreca, D.; Fornasiero, P. Enhanced Hydrogen Production by Photoreforming of Renewable Oxygenates Through Nanostructured Fe_2O_3 Polymorphs. *Adv. Funct. Mater.* **2014**, *24*, 372−378.
(17) Zhang, Q. F.; Uchaker, E.; Candelaria, S. L.; Cao, G. Z. Nanomaterials for energy conversion and storage. *Chem. Soc. Rev.* **2013**, *42*, 3127−3171.
(18) Singh, R. B.; Matsuzaki, H.; Suzuki, Y.; Seki, K.; Minegishi, T.; Hisatomi, T.; Domen, K.; Furube, A. Trapped state sensitive kinetics in $LaTiO_2N$ solid photocatalyst with and without cocatalyst loading. *J. Am. Chem. Soc.* **2014**, *136*, 17324−17331.
(19) Luan, P.; Xie, M. Z.; Liu, D. N.; Fu, X. D.; Jing, L. Q. Effective charge separation in the rutile TiO_2 nanorod-coupled α-Fe_2O_3 with exceptionally high visible activities. *Sci. Rep.* **2015**, *4*, 6180.
(20) Zhang, Z. Q.; Bai, L. L.; Li, Z. J.; Qu, Y.; Jing, L. Q. Review of strategies for the fabrication of heterojunctional nanocomposites as efficient visible-light catalysts by modulating excited electrons with appropriate thermodynamic energy. *J. Mater. Chem. A* **2019**, *7*, 10879−10897.
(21) Zhao, W.; Zhang, J.; Zhu, X.; Zhang, M.; Wang, Y. Enhanced nitrogen photofixation on Fe-doped TiO_2 with highly exposed (101) facets in the presence of ethanol as scavenger. *Appl. Catal., B* **2014**, *144*, 468−477.
(22) Tian, C. S.; Sheng, W. L.; Tan, H.; Jiang, H.; Xiong, C. R. Fabrication of lattice-doped TiO_2 Nanofibers by vapor-phase growth for visible light-driven N_2 conversion to ammonia. *ACS Appl. Mater. Interfaces* **2018**, *10*, 37453−37460.
(23) Schrauzer, G. N.; Guth, T. D. Photolysis of water and photoreduction of nitrogen on titanium dioxide. *J. Am. Chem. Soc.* **1977**, *99*, 7189−7193.
(24) Guan, R. Q.; Wang, D. D.; Zhang, Y. J.; Liu, C.; Xu, W.; Wang, J. O.; Zhao, Z.; Feng, M.; Shang, Q. K.; Sun, Z. C. Enhanced photocatalytic N_2 fixation via defective and fluoride modified TiO_2 surface. *Appl. Catal., B* **2021**, *282*, 119580.
(25) Zhang, Y. Z.; Chen, X.; Zhang, S. Y.; Yin, L. F.; Yang, Y. Defective titanium dioxide nanobamboo arrays architecture for photocatalytic nitrogen fixation up to 780 nm. *Chem. Eng. J.* **2020**, *401*, 126033.
(26) Zhang, G. Q.; Yang, X.; He, C. X.; Zhang, P. X.; Mi, H. W. Constructing a tunable defect structure in TiO_2 for photocatalytic nitrogen fixation. *J. Mater. Chem. A* **2020**, *8*, 334−341.
(27) Hirakawa, H.; Hashimoto, M.; Shiraishi, Y.; Hirai, T. Photocatalytic conversion of nitrogen to ammonia with water on surface oxygen vacancies of titanium dioxide. *J. Am. Chem. Soc.* **2017**, *139*, 10929−10936.
(28) Lan, K.; Wang, R. C.; Wei, Q. L.; Wang, Y. X.; Hong, A.; Feng, P. Y.; Zhao, D. Y. Stable Ti^{3+} Defects in Oriented Mesoporous Titania Frameworks for Efficient Photocatalysis. *Angew. Chem., Int. Ed.* **2020**, *59*, 17676.
(29) Andersen, S. Z.; Oli, V.; Yang, S.; Schwalbe, J. A.; Chorkendorff, I. A rigorous electrochemical ammonia synthesis protocol with quantitative isotope measurements. *Nature* **2019**, *570*, 504−508.
(30) Pei, D. N.; Gong, L.; Zhang, A. Y.; Zhang, X.; Chen, J. J.; Mu, Y.; Yu, H.-Q. Defective titanium dioxide single crystals exposed by high-energy {001} facets for efficient oxygen reduction. *Nat. Commun.* **2015**, *6*, 8696.
(31) In, S.-I.; Vaughn, D. D., II; Schaak, R. E. Hybrid CuO-$TiO_{2-x}N_x$ hollow nanocubes for photocatalytic conversion of CO_2 into methane under solar irradiation. *Angew. Chem.* **2012**, *124*, 3981−3984.
(32) Liu, J.; Yang, S.; Wu, W.; Tian, Q. Y.; Cui, S. Y.; Dai, Z. G.; Feng, R.; Xiao, X. H.; Jiang, C. Z. 3D Flower-Like α-Fe_2O_3@TiO_2 Core-Shell Nanostructures: General Synthesis and Enhanced Photocatalytic Performances. *ACS Sustainable Chem. Eng.* **2015**, *3*, 2975−2984.
(33) Zhang, Y.; Liu, H.; Jia, Y.; Deng, Y.; Li, S.; He, N. Y. A magnetic nanoparticles-based combination detection of COX-2 and BCL-2 polymorphisms associated with gastric cancer susceptibility. *Sci. Adv. Mater.* **2015**, *7*, 532−539.
(34) Palanisamy, B.; Babu, C. M.; Sundaravel, B.; Anandan, S.; Murugesan, V. Sol-gel synthesis of mesoporous mixed Fe_2O_3/TiO_2 photocatalyst: Application for degradation of 4-chlorophenol. *J. Hazard. Mater.* **2013**, *252*−*253*, 233−242.
(35) Pradhan, G. K.; Martha, S.; Parida, K. M. Synthesis of multifunctional nanostructured zinc-iron mixed oxide photocatalyst by a simple solution-combustion technique. *ACS Appl. Mater. Interfaces* **2012**, *4*, 707−713.
(36) Qin, D. D.; Wang, X. H.; Li, Y.; Gu, J.; Ning, X.-M.; Chen, J.; Lu, X.-Q.; Tao, C.-L. PH_3-treated TiO_2 Nanorods with Dual-doping Effect for Photoelectrochemical Oxidation of Water. *J. Phys. Chem. C* **2016**, *120*, 22195−22201.
(37) Zuo, F.; Bozhilov, K.; Dillon, R. J.; Wang, L.; Smith, P.; Zhao, X.; Bardeen, C.; Feng, P. Y. Active Facets on Titanium(III)-Doped TiO_2: An Effective Strategy to Improve the Visible-Light Photocatalytic Activity. *Angew. Chem., Int. Ed.* **2012**, *51*, 6223−6226.
(38) Lin, L.; Zheng, R. Y.; Xie, J. L.; Zhu, Y. X.; Xie, Y. C. Synthesis and characterization of phosphor and nitrogen co-doped titania. *Appl. Catal., B* **2007**, *76*, 196−202.
(39) Yu, J. C.; Ho, W.; Yu, J.; Yip, H.; Wong, P. K.; Zhao, J. C. Efficient Visible-Light-Induced Photocatalytic Disinfection on Sulfur-Doped Nanocrystalline Titania. *Environ. Sci. Technol.* **2005**, *39*, 1175−1179.
(40) Lei, X. F.; Xue, X. X.; Yang, H.; Chen, C.; Li, X.; Niu, M. C.; Gao, X. Y.; Yang, Y. T. Effect of calcination temperature on the structure and visible-light photocatalytic activities of (N, S and C) co-doped TiO_2 nano-materials. *Appl. Surf. Sci.* **2015**, *332*, 172−180.
(41) Hong, X. T.; Wang, Z. P.; Cai, W. M.; Lu, F.; Zhang, J.; Yang, Y. Z.; Ma, N.; Liu, Y. J. Visible-Light-Activated Nanoparticle

https://doi.org/10.1021/acssuschemeng.1c05890
ACS Sustainable Chem. Eng. XXXX, XXX, XXX−XXX

Photocatalyst of Iodine-Doped Titanium Dioxide. *Chem. Mater.* **2005**, *17* (6), 1548−1552.
(42) Gan, Q.; He, H.; Zhu, Y.; Wang, Z.; Qin, N.; Gu, S.; Li, Z.; Luo, W.; Lu, Z. Defect-Assisted Selective Surface Phosphorus Doping to Enhance Rate Capability of Titanium Dioxide for Sodium Ion Batteries. *ACS Nano* **2019**, *13*, 9247−9258.
(43) Shiraishi, Y.; Shiota, S.; Kofuji, Y.; Hashimoto, M.; Chishiro, K.; Hirakawa, H.; Tanaka, S.; Ichikawa, S.; Hirai, T. Nitrogen Fixation with Water on Carbon-Nitride-Based Metal-Free Photocatalysts with 0.1% Solar-to-Ammonia Energy Conversion Efficiency. *ACS Appl. Energy Mater.* **2018**, *1*, 4169−4177.
(44) Han, Q.; Wu, C. B.; Jiao, H. M.; Xu, R. Y.; Wang, Y. Z.; Xie, J. J.; Guo, Q.; Tang, J. W. Rational Design of High-Concentration Ti^{3+} in Porous Carbon-Doped TiO_2 Nanosheets for Efficient Photocatalytic Ammonia Synthesis. *Adv. Mater.* **2021**, *33*, 2008180.
(45) Ziarati, A.; Badiei, A.; Luque, R. Black Hollow TiO_2 nanocubes: advanced nanoarchitectures for efficient visible light photocatalytic applications. *Appl. Catal., B* **2018**, *238*, 177−183.
(46) Wang, S. Y.; Hai, X.; Ding, X.; Chang, K.; Xiang, Y. G.; Meng, X. G.; Yang, Z. X.; Chen, H.; Ye, J. H. Light-Switchable Oxygen Vacancies in Ultrafine Bi_5O_7Br Nanotubes for Boosting Solar-Driven Nitrogen Fixation in Pure Water. *Adv. Mater.* **2017**, *29*, 1701774.
(47) Wang, S. X.; Maimaiti, H.; Xu, B.; Guo, Y.; Zhai, P. S.; Zhang, H. Z. Fixation of nitrogen to ammonia with photocatalytic on petroleum pitch-based graphene oxide supported nickel/nickel oxide composite catalyst. *J. Phys. Chem. C* **2019**, *123*, 31119−31129.
(48) deKrafft, K. E.; Wang, C.; Lin, W. B. Metal-organic framework templated synthesis of Fe_2O_3/TiO_2 nanocomposite for hydrogen production. *Adv. Mater.* **2012**, *24*, 2014−2018.
(49) Naya, S.; Kimura, K.; Tada, H. One-Step selective aerobic oxidation of amines toimines by gold nanoparticle-loaded rutile titanium(IV) oxide olasmon photocatalyst. *ACS Catal.* **2013**, *3*, 10−13.
(50) Luan, P.; Xie, M. Z.; Fu, X. D.; Qu, Y.; Sun, X. J.; Jing, L. Q. Improved photoactivity of TiO_2-Fe_2O_3 nanocomposites for visible-light water splitting after phosphate bridging and its mechanism. *Phys. Chem. Chem. Phys.* **2015**, *17*, 5043−5050.
(51) Xie, M. Z.; Meng, Q. Q.; Luan, P.; Feng, Y. J.; Jing, L. Q. Synthesis of mesoporous TiO_2-coupled Fe_2O_3 as efficient visible nano-photocatalysts for degrading colorless pollutants. *RSC Adv.* **2014**, *4*, 52053−52059.
(52) Yang, J. H.; Guo, Y. Z.; Jiang, R. B.; Qin, F.; Zhang, H.; Lu, W. Z.; Wang, J. F.; Yu, J. C. High-Efficiency "Working-in-Tandem" Nitrogen Photofixation Achieved by Assembling Plasmonic Gold Nanocrystals on Ultrathin Titania Nanosheets. *J. Am. Chem. Soc.* **2018**, *140*, 8497−8508.
(53) Bolleter, W. T.; Bushman, C. J.; Tidwell, P. W. Spectrophotometric Determination of Ammonia as Indophenol. *Anal. Chem.* **1961**, *33* (4), 592−594.
(54) Dong, G. H.; Hob, W. K.; Wang, C. Y. Selective photocatalytic N_2 fixation dependent on g-C_3N_4 induced by nitrogen vacancies. *J. Mater. Chem. A* **2015**, *3*, 23435−23441.

https://doi.org/10.1021/acssuschemeng.1c05890
ACS Sustainable Chem. Eng. XXXX, XXX, XXX−XXX